Pore-scale water dynamics during drying and the impacts of structure and surface wettability

Brian C. Cruz[1] [iD], Jessica M. Furrer[2], Yi-Syuan Guo[3], Daniel Dougherty[3], Hector F. Hinestroza[2], Jhoan S. Hernandez[2], Daniel J. Gage[4], Yong Ku Cho[3], and Leslie M. Shor[3,5] [iD]

[1]Department of Civil and Environmental Engineering, University of Connecticut, Storrs, Connecticut, USA, [2]Department of Physics and Engineering, Benedict College, Columbia, South Carolina, USA, [3]Department of Chemical and Biomolecular Engineering, University of Connecticut, Storrs, Connecticut, USA, [4]Department of Molecular and Cell Biology, University of Connecticut, Storrs, Connecticut, USA, [5]Center for Environmental Sciences and Engineering, University of Connecticut, Storrs, Connecticut, USA

Abstract Plants and microbes secrete mucilage into soil during dry conditions, which can alter soil structure and increase contact angle. Structured soils exhibit a broad pore size distribution with many small and many large pores, and strong capillary forces in narrow pores can retain moisture in soil aggregates. Meanwhile, contact angle determines the water repellency of soils, which can result in suppressed evaporation rates. Although they are often studied independently, both structure and contact angle influence water movement, distribution, and retention in soils. Here drying experiments were conducted using soil micromodels patterned to emulate different aggregation states of a sandy loam soil. Micromodels were treated to exhibit contact angles representative of those in bulk soil ($8.4° \pm 1.9°$) and the rhizosphere ($65° \pm 9.2°$). Drying was simulated using a lattice Boltzmann single-component, multiphase model. In our experiments, micromodels with higher contact angle surfaces took 4 times longer to completely dry versus micromodels with lower contact angle surfaces. Microstructure influenced drying rate as a function of saturation and controlled the spatial distribution of moisture within micromodels. Lattice Boltzmann simulations accurately predicted pore-scale moisture retention patterns within micromodels with different structures and contact angles.

1. Introduction

Unsaturated soil exhibits dynamic hydraulic conditions governed by physically and biologically induced resistances to evaporation. Invasion of air into emptied pores proceeds according to pore size and capillary forces. Plants have developed a variety of adaptations to alter moisture dynamics and optimize water availability in the rhizosphere [*Carminati et al.*, 2016]. Mucilage, a polymeric gel secreted from plant roots, is capable of altering hydraulic conductivity [*Zarebanadkouki et al.*, 2015], shifting the moisture retention curve [*Carminati et al.*, 2010], and promoting soil particle aggregation [*Czarnes et al.*, 2000; *Traoré et al.*, 2000].

Plant mucilage acts as a hydrogel, swelling with water and increasing the equilibrium water content in the rhizosphere at a given matric potential, resulting in typically higher water contents within the rhizosphere versus bulk soil [*Carminati et al.*, 2010]. As mucilage dries out, however, it shrinks and binds to soil particles—hydrophobic functional groups, presented at the solid-vapor interface, increase soil water repellency (SWR) and soil contact angle. The combination of increased SWR and slow rewetting rate of mucilage results in reduced water content within the rhizosphere for days after rewetting [*Moradi et al.*, 2012]. The reduced moisture content during rewetting events serves to shield roots from extreme shifts in osmotic pressure [*Benard et al.*, 2016], while the increased moisture retention during dry conditions promotes plant resiliency. As mucilage ages within soil, hydrophobicity becomes increasingly permanent, which can lead to SWR independent of moisture content [*Carminati*, 2013]. Although SWR can be independent of moisture content, it is important to note that the previously described drying and rewetting behavior is not the result of permanent SWR, but rather the result of wetting properties that change with increasing and decreasing capillary pressure and moisture content.

Heterogeneous distribution of mucilage and organic matter results in a heterogeneous distribution of contact angles within soil [*Bachmann et al.*, 2013]; however, contact angles within the rhizosphere tend to be

higher versus those in bulk soil [*Moradi et al.*, 2012], resulting in greater hydrophobicity. The influence of increased contact angle on evaporation in soils is not fully understood [*Or et al.*, 2013]; however, studies on soils with mixed wettability [*Bachmann et al.*, 2001; *Shahidzadeh-Bonn et al.*, 2007] and hydrophobic layers [*Shokri et al.*, 2008] have observed suppressed evaporation compared to wettable media. Wettability differences between adjoining soil have been shown to drastically alter the macrodistribution of moisture in soil [*Shokri and Or*, 2013]. Two-dimensional pore network model simulations have demonstrated that contact angle can affect both drying time and kinetics [*Chapuis and Prat*, 2007; *Prat*, 2007]. Idealized square pore network models offer a simplified and controlled approach to understanding the effects of physical pore throat and size heterogeneity on multiphase systems; however, the physical heterogeneities of real soil are not fully captured within these models.

Secretion of mucilage in the rhizosphere promotes the formation of soil aggregates [*Czarnes et al.*, 2000]. Aggregated soil tends to contain an increased number of smaller pores with higher air entry pressures, and an increased number of larger macropores. The presence of smaller and larger pores promotes both gas exchange, and retention of water in soil aggregates. Mucilage may accumulate in the smallest pores, leading to higher SWR within rhizosphere micropores [*Ahmed et al.*, 2016]. Numerical models of root water uptake have increasingly incorporated the effects of mucilage on soil moisture [*Schwartz et al.*, 2016], however, little effort has been expended in incorporating the changes in SWR and soil structure due to the presence of organic mucilage into evaporation models. One powerful approach to study the effects of soil structure and SWR on evaporation is lattice Boltzmann modeling.

The lattice Boltzmann method (LBM) simulates fluid flow based on a discrete approximation of the Boltzmann equation and has become a powerful tool for simulation of microscale multiphase flow in porous media [*Ahrenholz et al.*, 2008; *Aidun and Clausen*, 2010; *Bao and Schaefer*, 2013]. LBM has been used to study infiltration and percolation phenomena in soils [*Li et al.*, 2005; *Sukop and Or*, 2003], as well as diffusive evaporation [*Chau and Or*, 2006; *Chau et al.*, 2005; *Haussels et al.*, 2001]. Using X-ray computed microtomography, studies have coupled experimental observations of real and artificial soil with LBM to determine pore-scale fluid distributions and movement [*Landry et al.*, 2014; *Sukop et al.*, 2008]. Microfluidic devices have been used to study both physical [*Karadimitriou et al.*, 2014, 2013; *Liu et al.*, 2011; *Pyrak-Nolte et al.*, 2008] and biological [*Markov et al.*, 2010a; *Olson et al.*, 2004; *Rubinstein et al.*, 2015; *Singh and Olson*, 2011; *Stanley et al.*, 2016; *Tang et al.*, 2013] pore-scale soil phenomena, and have been combined with LBM to evaluate fluid flow phenomena [*Dye et al.*, 2016; *Gray et al.*, 2015] and reactive transport [*Yoon et al.*, 2012] at the pore scale. Precise control of micromodel physical structure can be achieved, and devices cast in polydimethylsiloxane (PDMS) can be fabricated with similar surface properties to quartz sand [*Roman and Culbertson*, 2006]. Although LBM and microfluidics have proven useful in studying pore-scale soil processes, they have not been combined previously to study rhizosphere moisture dynamics.

Recently, we studied the influence of microbial mucilage, produced by the legume rhizosphere bacterium *Sinorhizobium meliloti*, on soil drying kinetics using a soil micromodel emulating the structure of a sandy loam soil [*Deng et al.*, 2015]. Results indicated that mucilage produced by bacteria promoted slower drying rates and increased drying times, but only within a microstructured environment. In this study, our objectives were to (i) determine whether soil microstructure or wettability had a greater effect on evaporative drying kinetics in porous media and (ii) validate a lattice Boltzmann method (LBM) model for studying moisture distribution and drying kinetics in our micromodels. Contact angle in soil is dynamic and changes with moisture content; however, this behavior can be difficult to replicate. Our study focused on using two contact angles which represent the differences in wettability between bulk and rhizosphere soil. Drying experiments were conducted using pseudo-two-dimensional soil micromodels modified to emulate the physical restructuring and wettability differences between the rhizosphere and bulk soil. Each micromodel was patterned to emulate the microstructure of a sandy loam soil in different aggregation states, and modified through plasma activation to have different contact angles. A lattice Boltzmann model was developed to simulate the effects of pore microstructure changes and contact angle variations on drying and moisture distribution within our micromodels, and validated with experimental results.

2. Materials and Methods

2.1. Micromodel Design and Fabrication
Pseudo-two-dimensional emulated soil micromodels were fabricated from two-dimensional (2-D) micromodel patterns using standard methods of photolithography and soft lithography as previously described

[*Deng et al.*, 2013; *Markov et al.*, 2010a, 2010b]. Micromodel patterns were designed with three identical channels each containing a 1 mm × 1 cm soil microstructure region. Two different micromodel patterns were used to emulate aggregated and nonaggregated soil microstructures, respectively. Both aggregated and nonaggregated micromodel microstructure patterns were derived from a three-dimensional (3-D) random packing of ellipsoidal particles whose diameters were based on measured particle diameters of a sieved sandy loam soil with porosity 0.52 [*Deng et al.*, 2015]. 2-D particle distributions were identical between micromodel patterns and consistent with particle distribution of a sieved sandy loam soil [*Deng et al.*, 2015; *Furrer and Bagtzoglou*, 2017] (supporting information Figure S1a); however, aggregated micromodel particle positions were manipulated to generate aggregates of particles (250 μm to 2 mm diameter). With different particle positions, the pore geometries between nonaggregated and aggregated micromodels were different, resulting in difference in their pore size distributions (supporting information Figure S1b). Aggregated micromodels exhibited larger (>100 μm) and smaller (< 20 μm) pore radii versus nonaggregated micromodels. Pore radii were estimated as the maximum radii of circles which could be inscribed between particles in a 2-D plane [*Münster and Fabry*, 2013], while particle diameters were estimated as equivalent diameters; both were calculated using MATLAB (Mathworks, Natick MA). Fabricated micromodel channels were 34.5 ± 2.5 μm tall, and micromodels were composed of polydimethylsiloxane (PDMS, Sylgard 184, Dow Corning, Midland, MI) castings bound to glass slides.

PDMS and glass slides were cleaned with isopropyl alcohol and methanol, respectively, dried at 60°C for at least 1 h, cooled to room temperature, then exposed to oxygen plasma for 30 s (Harrick PDC-32G, 18W RF Coil, Harrick Plasma, Ithaca, NY). Micromodels used for low contact angle (hydrophilic) experiments were filled immediately with DI water. High contact angle (hydrophobic) micromodels were stored at 60°C for 24 h and allowed to reach room temperature before being filled by perfusion with DI water. PDMS and glass slide contact angles were captured using a Dino Lite Edge digital microscope set up as a goniometer, then measured using an ImageJ plugin [*Stalder et al.*, 2006]. Low and high contact angles were measured, in triplicate, as 8.4° ± 1.9° and 65° ± 9.2°, respectively (supporting information Figure S2), and are described here as low water repellency (LWR) and high water repellency (HWR), respectively.

2.2. Drying Experiments

Micromodels filled with DI water were placed horizontally, so as to remove gravity effects, within a custom built control chamber which was kept under consistent relative humidity (RH) conditions [*Deng et al.*, 2015]. Micromodel wells were punched on both sides of the microfluidic device using a 4 mm biopsy punch, allowing evaporation from both sides of the micromodel channels. Experiments were conducted in triplicate, with two micromodel devices in each experiment. Each device contained three replicate microchannels, resulting in data from six microchannels per experiment. The two micromodels used in each LWR experiment were the same microstructure pattern as each other (both aggregated or both nonaggregated). HWR experiments were conducted slightly differently due to increased variability in RH; the two micromodels used were each a different microstructure pattern (aggregated and nonaggregated). This ensured differences in drying between micromodels were not caused by variations in RH. An Oasis Excel humidifier was used to regulate humidity, and both RH and temperature were measured using a MSR humidity and temperature data logger. An experimental schematic (supporting information Figure S3) and summary of RH conditions (supporting information Table S1) can be found in the supporting information.

The control chamber was mounted horizontally on an AxioObserver Z1 AX10 inverted wide field microscope (Carl Zeiss, Oberkochen, Germany) and mosaic images of microstructured micromodel channels were taken at 5X magnification. Images were captured every 20 min for the length of each experiment. Data from 18 microchannels in total were collected from the triplicate experiments. Some conditions are reported with data from less than 18 replicates due to channel obstructions from debris introduced during device bonding or filling. If micromodel channels were obstructed by debris introduced during bonding/filling, or micromodel drying occurred from within the microstructure region due to trapped vapor bubbles within pores, all images for the channel were excluded from analysis.

2.3. Lattice Boltzmann Method (LBM): Model Formulation

The lattice Boltzmann method is a fluid dynamics modeling methodology that computes the evolution of particle distributions on a lattice. It accurately reproduces solutions to the Navier-Stokes equations in simple geometries [*Qian et al.*, 1992] and is highly adaptable to simulation of fluid behavior in complex geometries

such as soil. A single-component multiphase LBM model was used to simulate moisture dynamics within the microfluidic micromodels.

The LBM has been extensively described elsewhere [*Martys and Chen*, 1996; *Qian et al.*, 1992; *Shan and Chen*, 1994; *Zou and He*, 1997], including the development of the current implementation [*Chau et al.*, 2005] but we give a brief overview here. Particle distributions f_i move on a lattice according to the lattice Boltzmann equation:

$$f_i\left(\vec{x}+\hat{e}_i,\ t+1\right)-f_i\left(\vec{x},t\right)=-\frac{1}{\tau}\left[f_i\left(\vec{x},t\right)-f_i^{eq}\left(\vec{x},t\right)\right] \tag{1}$$

which describes the processes of streaming (movement toward neighboring nodes) and collision (in which particle distributions relax toward a Gaussian equilibrium distribution, unless impacted by other factors). Here f_i represents the direction-specific particle density at lattice node x, $\hat{e}_i$ are the lattice velocity vectors, τ is a relaxation parameter, t is the time step, and f_i^{eq} is the equilibrium distribution at each node. The macroscopic quantities of density and velocity for each node are obtained by summing the direction-specific densities and momenta as follows:

$$\rho\left(\vec{x},t\right)=\sum_i f_i\left(\vec{x},t\right) \tag{2}$$

$$\vec{u}\left(\vec{x},t\right)=\frac{\sum_i f\left(\vec{x},t\right)\hat{e}_i}{\rho\left(\vec{x},t\right)} \tag{3}$$

Our code is implemented in 2-D, and simulates a single fluid, capable of evaporation and condensation (single-component, nonideal gas equation of state) following *Sukop and Or* [2004]. It employs the following potential function:

$$\Psi(x,t)=\ \Psi_0\exp\left[-\frac{\rho_0}{\rho(x,t)}\right] \tag{4}$$

with $\psi_0 = 4$ and $\rho_0 = 200$ [*Martys and Chen*, 1996; *Shan and Chen*, 1994]. The potential function is used to modify the velocity in the equilibrium distribution, in order to include nonideal gas interactions (interaction between liquid and solid phases) [*Shan and Chen*, 1994]. Fluid-solid interactions (wettability) are also implemented as a modification to the equilibrium distribution f_{eq} according to *Shan and Chen* [1994].

Wetting behavior in the LBM code is implemented as a local applied acceleration toward neighboring solid nodes following *Luo* [2000], the magnitude of which is controlled by the wetting parameter $G_{adsorption}$. Contact angles were determined for different values of $G_{adsorption}$ by running simple simulations (liquid droplets on solid surfaces) to equilibrium, then measuring the contact angle of the resulting liquid configuration using the half-angle method. $G_{adsorption}$ was varied from 0.02 to 0.10 to achieve wetting and nonwetting conditions within LBM simulations. Values of $G_{adsorption}$ of 0.08 and 0.06 corresponded to contact angles of 6° and 72°, respectively (supporting information Figure S4). These were tuned to mimic the LWR (contact angle 8.4° ± 1.9°) and HWR (contact angle 65° ± 9.2°) experimental conditions in soil micromodels.

2.4. LBM Implementation
Evaporation simulations were performed in geometries identical to those of the aggregated and nonaggregated micromodels. Microscope images of micromodels were converted to bitmaps with a scale of 10 μm per lattice unit (lu), or pixel. Bitmaps showing 2-D soil particles as impermeable solid nodes were converted to x–y coordinate datafiles with MATLAB and used as boundary conditions for the LBM simulations.

A single nonideal fluid capable of evaporation and condensation was initially distributed evenly throughout the computational domain, with density values representing the liquid phase. (This is analogous to the initially saturated condition in micromodel drying experiments.) Simulations were set up with constant density (pressure) boundary conditions at the left and right of the domain and periodic boundaries on the top and bottom. This is analogous to prescribing the relative humidity at the boundaries of the soil micromodels. The boundary density values were identical for the left and right boundaries and were constant in time throughout the simulations. Density boundary values were equivalent to dry soil air, producing simulations

in which liquid evaporated out through the boundaries and was replaced by the invading vapor phase. Simulations were run until the computational domain was completely vapor filled, or until no further change (to within a precision of 10^{-10}) in the total system mass and velocities were detected.

Simulations were performed to represent all experimental treatments: aggregated and nonaggregated geometries, each at a solid-liquid contact angle of 6° (LWR) and 72° (HWR). Additionally, simulations were performed at a range of boundary densities, representing different ambient relative humidity conditions. As expected, the evaporation behavior of the simulations varied according to the boundary conditions applied.

2.5. Analysis of Drying in Experiments and LBM Simulations

Analysis of drying experiment images was performed as previously described [*Deng et al.*, 2015], with slight modification. Using ImageJ version 1.51d, with the open source Fiji image-processing package [*Schindelin et al.*, 2012], a threshold was applied to each mosaic image of the 1 mm × 1 cm microstructure region. The threshold allowed the continuous vapor interface along hydrated pore spaces or PDMS pillars to be resolved. The vapor-phase area behind the vapor-liquid or vapor-PDMS interface was manually filled with red pixels using the position of the vapor-liquid interface as a guide. Each image was converted to an 8 bit gray-scale image and, by applying a threshold, the red colored vapor area was selected for analysis. The selected area constituted the vapor-phase area within the microstructured region of each microchannel. The images used contained portions of micromodel channels outside the 1 mm × 1 cm microstructure region; unstructured portions were subtracted from the total measured area of their respective images. Micromodel saturation was calculated using the ratio of vapor area to total pore area:

$$S = 1 - \frac{A_V - A_C}{A_T - A_C} \tag{5}$$

where S is saturation, A_V is the vapor-phase area, A_C is the area of the channel in each image outside the 1 mm × 1 cm microstructure region, and A_T is the total area of pore space within the micromodel.

Saturation and residual saturation values for LBM simulation images were computed using MATLAB and were based on the porosity of the micromodels.

Micromodel channels exhibited variation in the time needed for the invading vapor phase to reach the microstructured region. The starting point of drying was defined as the time at which the vapor phase reached both edges of the microstructure region, and the change in saturation was greater than 1%. In the experiments, all micromodels dried completely to within an experimental precision of ± 1%.

Drying rate [μg min^{-1}] in micromodel experiments was computed by dividing the mass of liquid lost to evaporation between consecutive time points by the elapsed time:

$$\text{Drying rate}_{t=n} = \frac{Mass_{t=n-1} - Mass_{t=n}}{t_n - t_{n-1}} \tag{6}$$

Equilibrium time (t_{eq}) in experiments was determined as the time at which change in saturation was less than 1%, which reflected the lowest change in saturation which could be analyzed reliably using our image processing method. Lattice Boltzmann equilibrium time was determined as the time at which no further change in fluid content or configuration was occurring (no further change in total system mass and velocity).

Since the precision of the simulation far exceeded the precision of experiments, we also defined an "apparent equilibrium" to exclude long flat "tails" in the simulations when comparing characteristic drying behavior between simulations and experiments. In this case, the convergence criterion for "apparent equilibrium" was the twentieth consecutive time step where the change in saturation was less than 1% of the current saturation.

Drying rates were compared and significance of results was estimated using a two-tailed Student's t test for unpaired data.

Simulations with density boundary conditions (DBCs) of 50, 60, 65, 70, 72, 74, 76, and 78 mu/lu^2 were performed, and these data were analyzed to identify which DBC best captures the characteristic drying behavior

of the experimental data. Experiments and simulations were compared on a relative time basis; each was normalized from 0 to 1, where 1 is the time the device was dry in experiments, or the apparent equilibrium time step of the simulation. A high order ($4 \leq n \leq 7$) polynomial equation was fit to LBM simulations using the EZFIT toolbox in MATLAB. The best fit polynomial was then used to compare saturation of the experiment at each relative time to the saturation of the simulation at the same relative time. A sum of squared errors analysis showed that DBC = 74 mu/lu^2 provided the best match for experimental data. Therefore, lattice Boltzmann simulations with DBC = 74 mu/lu^2 will be the focus of the subsequent discussions and analysis.

2.6. Analysis of Vapor Infiltration Patterns Within Micromodels

Evolving vapor infiltration patterns within the microstructured regions of micromodels and in LBM simulations were quantitatively compared using a characteristic liquid-vapor interface length. Characteristic length (L_c) of the liquid-vapor interface was defined as the observed vapor-phase area divided by the liquid-vapor interface length:

$$L_c = \frac{A_V - A_C}{P_{L-V}}$$

(7)

where A_V is the vapor-phase area, A_C is the area of the channel in each image which does not contain microstructures, and P_{L-V} is the perimeter of the vapor phase (liquid-vapor and vapor-PDMS interface). Area and perimeter values were measured using a macro in Fiji which applied a threshold to colored images. The characteristic length represents the shape of the vapor invasion front into the soil microstructure. The value of L_C is low if vapor infiltrated into multiple pores evenly and moved as a drying front by wrapping around individual PDMS "particles." The value of L_C is high for finger-like invasion fronts which infiltrated between particles but did not wrap completely around them.

To compare vapor infiltration patterns between experiments and simulations, the parameter L_{Norm} was defined, where L_{Norm} is L_C divided by the total vapor-PDMS interfacial length within the microstructure region. Normalizing characteristic length provided a dimensionless parameter which was unaffected by slight differences in total pore area or particle size differences between experimental and simulated micromodels. Values of normalized characteristic length >1 indicated vapor had infiltrated into the microstructured region of the micromodel but did not infiltrate into the smallest pore spaces, while values of ≤1 indicated uniform vapor infiltration into both large and small pore spaces. Normalized characteristic length of all micromodels started at a value of 0, since no vapor had begun infiltrating into the microstructure region, and converged at a value of 1 when fully dried.

3. Results

3.1. The Influence of Micromodel Structure and Water Repellency on Drying Rate

Differences in drying time in the micromodels were most influenced by water repellency, with high water repellency (HWR) micromodels taking approximately 4 times as long to dry versus low water repellency (LWR) micromodels (Table 1). Also, drying rates changed as micromodels dried (Figure 1). At saturation values higher than 0.5, LWR aggregated micromodels exhibited periods of rapid drying, during which drying rate was significantly higher ($p < 0.001$) versus LWR nonaggregated micromodels across the same saturation range (Figure 1). At saturation values lower than 0.25, LWR aggregated micromodels dried significantly slower ($p < 0.001$) versus LWR nonaggregated micromodels. HWR micromodels showed no statistically significant difference in drying rate at evaluated saturation values (supporting information Table S2). Both HWR and LWR aggregated micromodels exhibited significantly lower drying rate at low (0.25–0) versus high

Table 1. Drying Times for Micromodels[a]

Micromodel Pattern	Contact Angle[a] (°)	Drying Time[b] (h)[c]	Number of Replicate Microchannels
HI aggregated	8.4 ± 1.9	4.7 ± 0.8[i]	17
HI nonaggregated	8.4 ± 1.9	5.0 ± 0.6[i]	18
HO aggregated	65 ± 9.2	21.7 ± 5.1[ii]	15
HO nonaggregated	65 ± 9.2	19.9 ± 5.3[ii]	13

[a]Mean ± standard deviation, n = 3.
[b]Mean ± standard deviation of the number of replicates indicated in the next column.
[c]Drying times with the same superscript (i and ii) are not statistically different, while those with a different superscript are different at $p < 0.05$ (Student's t test, two tailed).
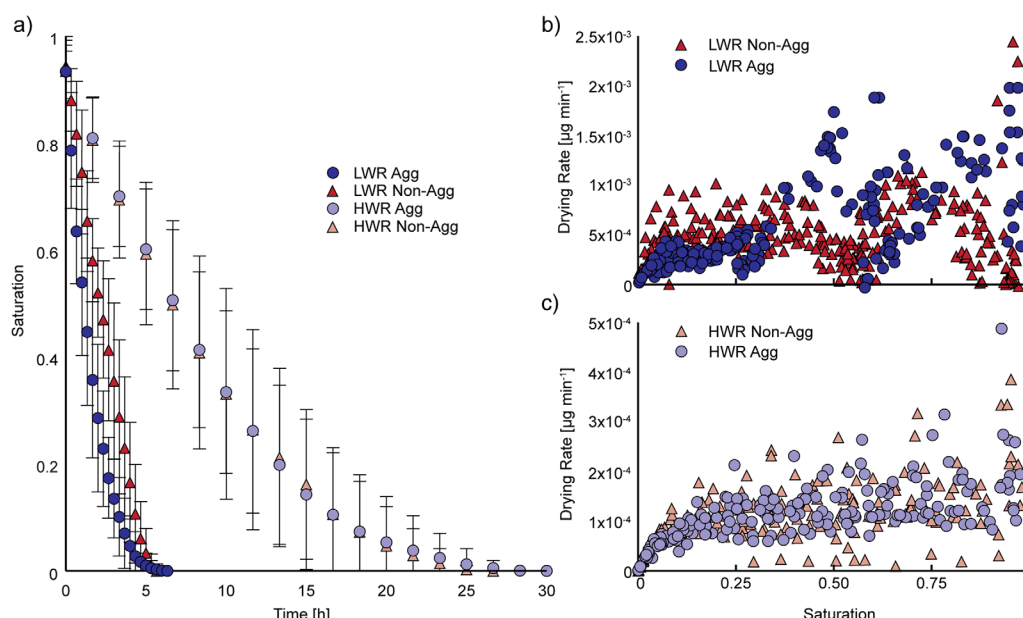
Figure 1. (a) Change in saturation versus time within micromodels illustrates the impact of contact angle on drying time. Differences in drying rate with micromodel saturation are compared between aggregated (Agg) and nonaggregated (Non-Agg) soil micromodels with (b) low water repellency (LWR), and (c) high water repellency (HWR) surfaces. HWR micromodels dried much slower versus LWR micromodels.

(1–0.75) saturation (supporting information Table S3). HWR nonaggregated micromodels also showed a significantly different drying rate at low versus high saturations; however, LWR nonaggregated micromodels did not show such a difference.

3.2. Lattice Boltzmann Simulation Results

In the LBM simulations, the density boundary conditions (DBCs) are analogous to prescribing the ambient relative humidity at the boundary of the soil micromodel. Simulations were conducted over a range of density boundary conditions (DBCs = 50–78 mu/lu^2) corresponding to lower (50 mu/lu^2) and higher relative humidity values (78 mu/lu^2). Density boundary conditions were varied to examine the effects of RH on drying within the two geometries (aggregated and nonaggregated). Higher DBC simulations, regardless of micromodel aggregation or water repellency, resulted in drying requiring more time steps (Figure 2). In low water repellency simulations, higher DBC values (higher RH) resulted in larger residual saturations at equilibrium (Figure 2). Simulations at the lowest DBC values (low RH) dried completely, mimicking the micromodel experiments which were conducted at RH $\approx$ 80%. In high water repellency simulations, all DBC values dried completely.

The structure of the simulated soil geometry (aggregated versus nonaggregated) had the largest effect on drying behavior in the LBM simulations. For DBC = 74 mu/lu^2, the LWR aggregated simulation dried in 3.0 times faster than the corresponding nonaggregated simulation, and 3.2 times faster for the HWR condition (Figure 2). A similar effect was observed under other RH conditions: the aggregated simulations dried 3.1–3.2 times faster for DBC = 70 mu/lu^2, and 3.4 times faster for DBC = 50 mu/lu^2.

Drying rates were calculated numerically for each DBC condition (Figure 2). The highest drying rates were observed at saturations close to 1 (at the beginning of the simulations, when the ambient RH boundary was closest to the invading air front). Rates decreased steadily throughout the aggregated simulations, tapering off toward the end of the simulations as the saturation approached zero. In the nonaggregated simulations, the drying rate dropped quickly after the initial vapor front invasion, and proceeded at a relatively constant level as the simulations proceeded toward zero saturation.

3.3. Lattice Boltzmann Simulations Reproduce Drying Behavior

Lattice Boltzmann method simulations at DBC = 74 mu/lu^2 (Figure 2c) were compared with drying experiment results using a dimensionless time scale, by plotting saturation versus relative time (Figure 3). This
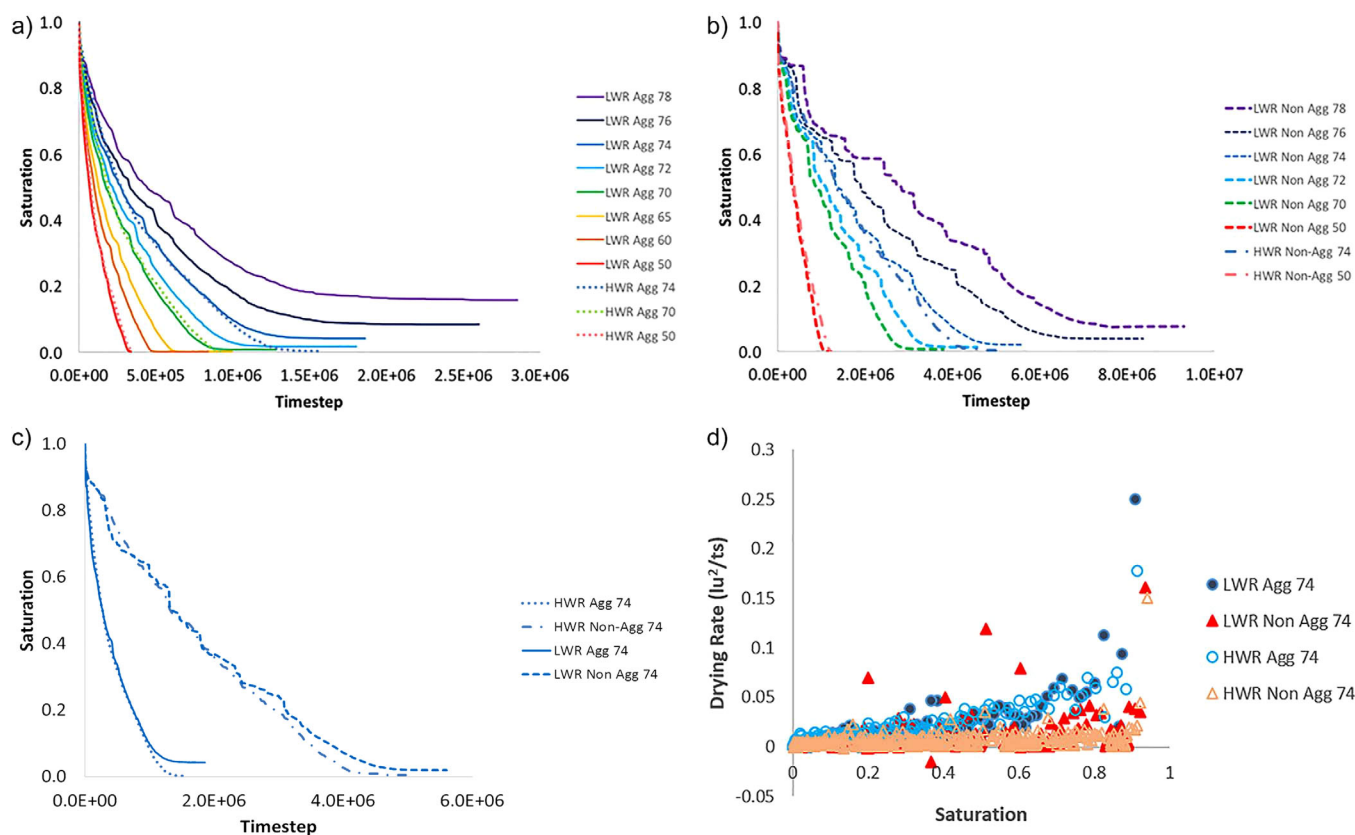
Figure 2. Simulated drying kinetics showing saturation versus Lattice Boltzmann method (LBM) time step for both high and low water repellency (HWR and LWR, respectively) for (a) aggregated (Agg) and (b) nonaggregated (Non-Agg) micromodels. Drying was simulated at different relative humidities (RH) by varying the density boundary condition (DBC) from DBC = 50 mu/lu^2 (driest) to DBC = 78 mu/lu^2 (wettest). (c) Comparison of drying kinetics for the DBC = 74 mu/lu^2 condition that best fits the experimental data. (d) Simulated drying rate as a function of saturation.

was the boundary condition that best matched the experimental drying behavior. Simulations with higher DBC values resulted in greater residual saturation which was unrealistic compared to our experiment observations. Other simulations that dried completely (DBC = 50, 60, and 65 mu/lu^2) resulted in higher sum of squared errors when fitted to the experimental data, as described in section 2.5.

Simulations with DBC = 74 mu/lu^2 of low and high water repellency within aggregated and nonaggregated micromodels generally reproduced experimental drying curves (Figure 3), with the LWR aggregated and HWR nonaggregated cases being closest to the experimental data. Treatments exhibiting the greatest curvature indicate drying rates that are strong functions of saturation. In light of this, the LWR aggregated and nonaggregated drying rates were slightly overestimated as a function of saturation.

LBM simulations of aggregated and nonaggregated structures with LWR and HWR surface properties found that drying in aggregated structures, regardless of water repellency, was a stronger function of saturation versus drying in nonaggregated structures. In other words, drying in nonaggregated soil geometry (both micromodel and experiments) proceeded at a relatively constant rate, regardless of saturation. This is a result of the relative flatness of the drying front in the nonaggregated case, which will be discussed further in section 4.1.

LBM simulations captured the characteristic microscale patterns of vapor infiltration across all pore geometries and water repellency conditions (Figure 4). At each saturation, the geometry of the modeled invading vapor front matched very closely with the corresponding experimental observation, indicating that the model accurately captured the physics of nonwetting phase invasion into the simulated soil. In order to quantify this match, LBM infiltration patterns were compared with experimental observations using a normalized characteristic length (L_{norm}), which depended on the shape of the vapor phase within each micromodel. At higher saturation values, the largest connected pores of the aggregated micromodels dried first
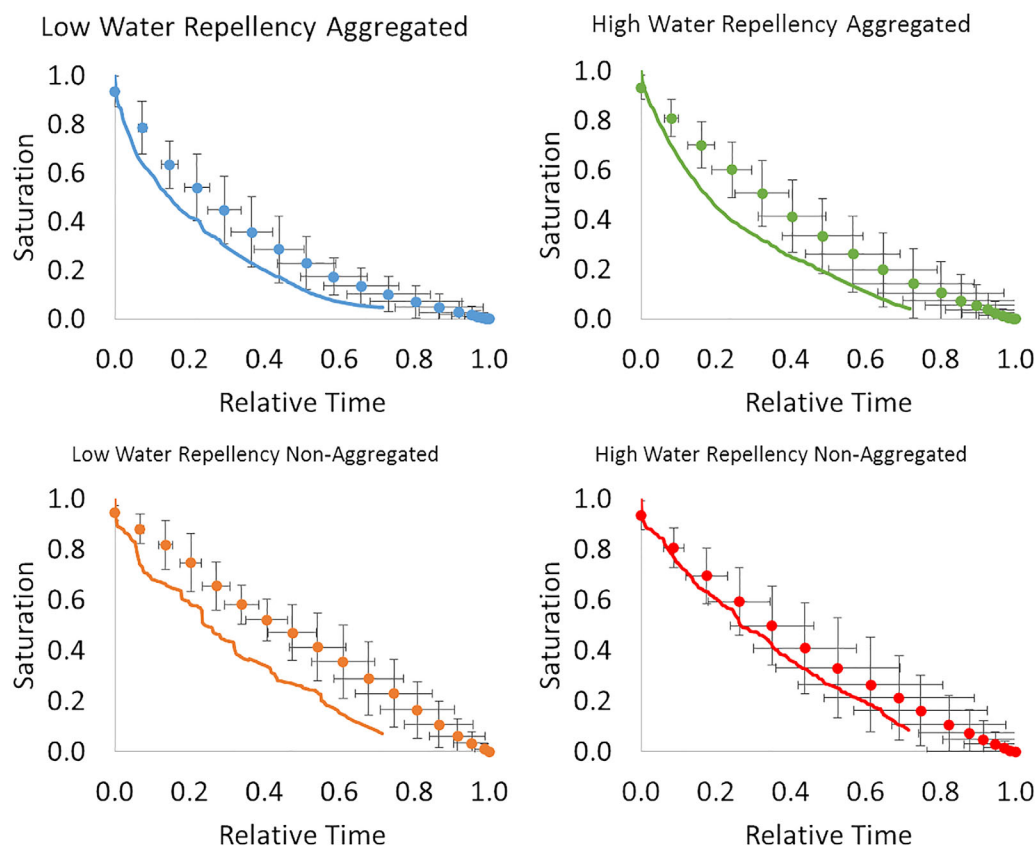
Figure 3. Experimentally measured drying kinetics versus lattice Boltzmann method (LBM) simulations with density boundary condition (DBC) = 74 mu/lu^2 for micromodels with high and low water repellency and aggregated and nonaggregated geometry.

which resulted in an elongated vapor phase that was constrained within the central portion of the micromodel (Figure 4), and values of $L_{norm} > 1$ (Figure 5). In nonaggregated micromodels, vapor infiltrated in a more uniform manner and moved as a front through the micromodel (Figure 4), resulting in $L_{norm} \leq 1$. LBM normalized characteristic length calculations for HWR micromodels generally followed experimental observations; however, LBM simulations underestimated LWR aggregated micromodel normalized characteristic length at higher saturations, and overestimated it at lower saturations. These variations may have been caused by the threshold which was applied to differentiate the vapor and liquid phases in simulations. Modification of these parameters could lead to more accurate representations of vapor infiltration behaviors.

4. Discussion

We chose contact angles representative of those found in bulk soil and the rhizosphere and studied their effects independently and in conjunction with changes in soil microstructure. Our relative humidity conditions (~80%) are too dry to directly relate our results to evaporative drying in the rhizosphere; however, experimental results indicate that changing water repellency drastically changes evaporative drying rate, and that microstructure controls the spatial distribution of soil moisture. LBM simulations of soil moisture distribution were validated for low and high water repellency conditions and different geometries. Once validated, the model allows for exploration of a wider range of RH and water repellency conditions than are possible experimentally. We now have the capability to investigate more rhizosphere-relevant relative humidity conditions, as well as spatially distributed water repellency conditions.

4.1. Microscale Patterns of Moisture Retention
Vapor infiltration into soil follows an invasion percolation behavior [*Sukop and Or*, 2003] wherein the nonwetting fluid (vapor) first invades the largest pores, where capillary forces are weakest. Qualitative analysis of vapor infiltration into each soil micromodel pattern was important to demonstrate that the LB model
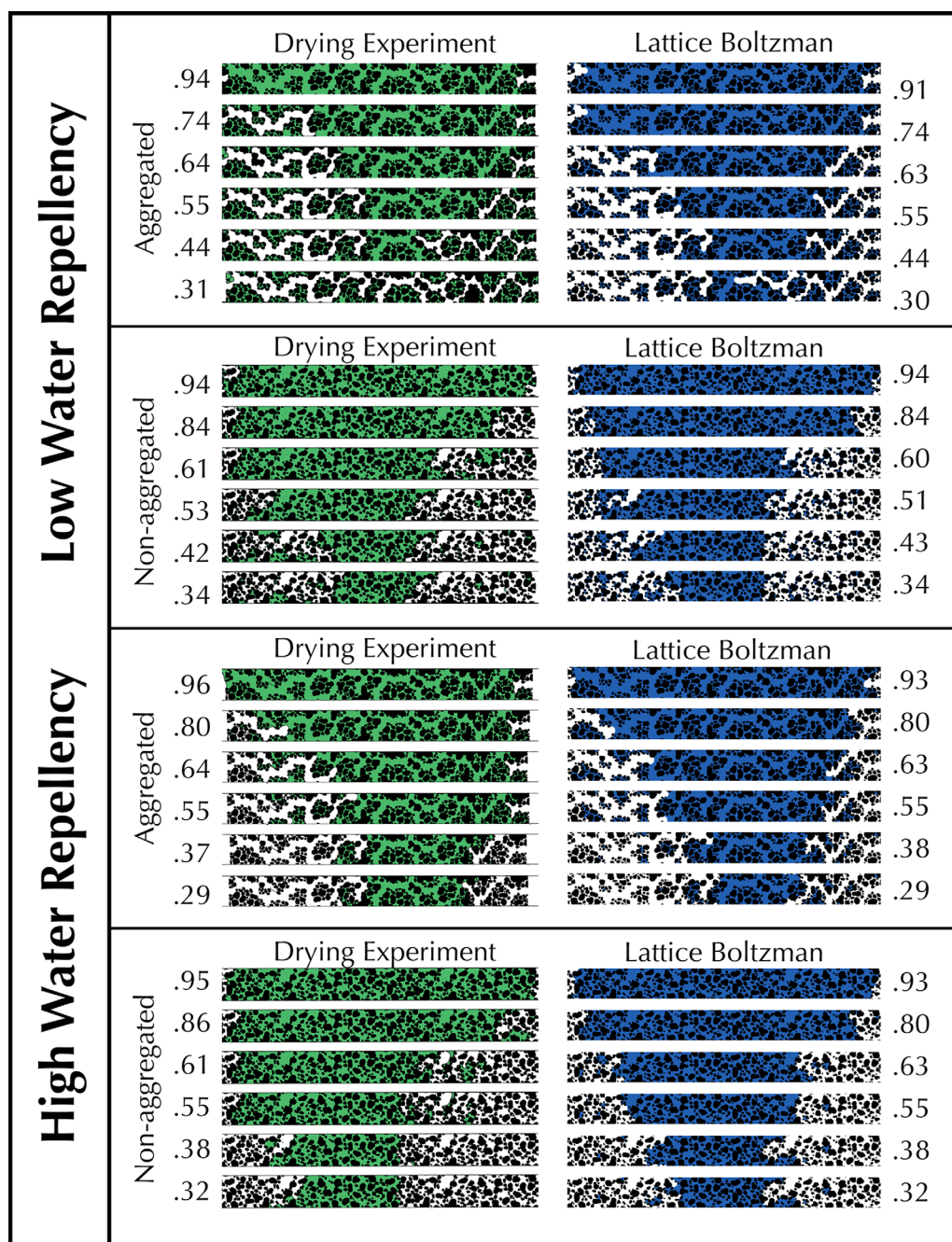
Figure 4. Comparison between observed (drying experiment) and simulated (Lattice-Boltzmann) pore-scale water distribution for low and high water repellency and aggregated and nonaggregated geometry. Snapshots are ordered based on saturation to illustrate variation in air infiltration patterns and the spatial distribution of water, where the number to the side of each image indicates saturation for that frame.

could predict micro-scale changes in water distribution in an emulated soil micromodel. Micro-scale progression of the vapor interface during drying was constrained by the microstructured features of each micromodel. Differences in particle positions and pore distributions between the aggregated and nonaggregated micromodels resulted in distinct vapor infiltration patterns which were qualitatively well replicated by the simulations (Figure 4). The presence of large interconnected pores in the aggregated micromodels led to a distinctly different pattern of vapor infiltration versus that in nonaggregated micromodels. Micro-scale patterns of the invading vapor phase were also highly dependent on contact angle.
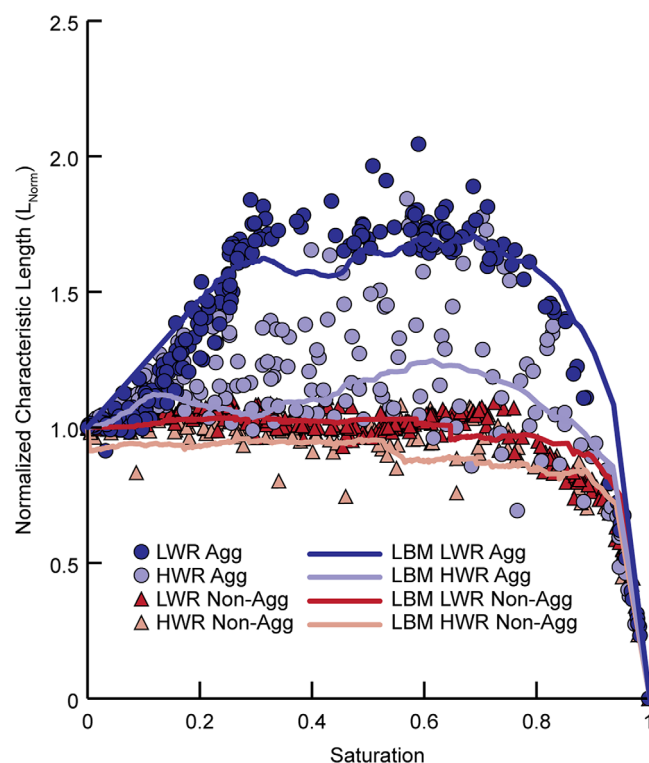
Figure 5. Normalized characteristic length (L_{norm}) values represent a quantitative measure of vapor infiltration patterns as micromodels dried (decreased saturation). L_{norm} from aggregated (Agg) and nonaggregated (Non-Agg) drying experiments are compared to lattice Boltzmann method (LBM) simulations. Values of normalized characteristic length >1 indicated vapor had infiltrated into the microstructured region of the micromodel but did not infiltrate into the smallest pore spaces, while values of ≤ 1 indicated uniform vapor infiltration into both large and small pore spaces.

Low water repellency (LWR) aggregated micromodels and simulations exhibited an initial drying period during which only the largest connected pores (80–300 μm) were emptied and the micropores (20–80 μm) within aggregated groups of particles remained saturated. Once the larger pores were completely dried, intraaggregate micropores began drying and continued until the micromodel was fully dried (Figure 4). This effect was mitigated under very dry density boundary conditions (DBCs = 50–65 mu/lu^2). More intense drying conditions at the boundaries resulted in micropores drying before the front had progressed through the simulated soil (supporting information Figure S6).

Drying behavior within high water repellency (HWR) aggregated micromodels were unique as well: although the largest connected pores appeared to empty first, intraaggregate micropores also began drying before the largest pores had completely dried (Figure 4). LWR and HWR nonaggregated micromodels exhibited infiltration from both sides of the micromodel in an alternating but relatively uniform pattern (Figure 4), as previously described [*Deng et al.*, 2015]. The vapor-phase infiltration from either side was controlled by the sizes of available pore throats, and the vapor interface often appeared to stop advancing on one side of the micromodel while continuing to advance on the other side. LBM simulations replicated experiment observations both qualitatively and quantitatively; however, variations occurred including different timing of advancement of the drying front from the two sides of the soil micromodel (Figure 4). The model replicated the patterns of advancement, but in many cases the left side of the model advanced before the corresponding experiment did so, relative to the position of the right side. This variation may be attributed to slight temperature and RH variations present in real-life experiments; in this case the constant DBC in the model may be regarded as the more reliable indicator of behavior under constant RH conditions. Micron-scale differences between pore structures of devices and simulation patterns, and heterogeneity in surface wettability within experiments are other possible causes of the discrepancies.

Pore-scale phenomena were observed in drying experiments including Haine's jumps and fluid retraction events [*Armstrong et al.*, 2015]. A Haine's jump is a rapid infiltration of vapor into pores which is a result of both fluid displacement and evaporation. Within LWR aggregated micromodels, a Haine's jump sometimes occurred just before vapor reached both sides of the microstructure region. The vapor interface would advance partially into the microstructure region, then stop at a pore constriction until vapor entered from the other side. This resulted in a reduced initial saturation, since drying was not tracked until the vapor interface was present at both sides of the microstructure region. Haine's jump likely occurred in aggregated micromodels because the largest pores allowed conductance of water by flow and did not have high enough capillary forces to prevent vapor entry by fluid displacement. Fluid retraction events, characteristic of interfacial jumps [*Moebius and Or*, 2012], were also observed during drying: as vapor entered a pore the liquid-vapor interface would retract from other pore throats.

4.2. Effects of Water Repellency and Soil Structure on Drying

Structured soil tends to retain moisture better versus unstructured soil [*Tracy et al.*, 2015], and water is held most tightly within the interstitial spaces of soil microaggregates [*Or et al.*, 2007]. Studies have shown soils with mixed wettability dry slower [*Shokri et al.*, 2009a]; however, this is the first study to compare the relative effects of both wettability and pore microstructure on drying. Water repellency drastically changed drying rates within soil micromodels and mediated the effects of microstructure differences on drying rates. High water repellency (HWR) micromodels took nearly 4 times longer to fully dry versus low water repellency (LWR) micromodels. The LBM model captured the drying behavior differences between low water repellency and high water repellency micromodels. Regardless of structure, HWR simulations dried slower than LWR simulations.

This finding suggests that film flow and the shape of the vapor-liquid interface had a significant influence on evaporative drying within our micromodels. Capillary driving forces and water films are affected by changes in wettability [*Shokri et al.*, 2009b]. Our HWR contact angle was above the critical contact angles predicted by *Prat* [2007], suggesting the presence of liquid films in LWR micromodels and the absence of films in HWR micromodels. We observed the persistence of water films in LWR micromodels but not in HWR micromodels (supporting information Figure S5), indicating the reduced evaporation in HWR micromodels may have been caused by disconnection of water films. Disconnection of water films is characteristic of shifting from stage 1 evaporation (capillary driving forces dominant) to stage 2 (diffusion dominant) and is typically marked by a substantial reduction in drying rate [*Shokri and Or*, 2011]. As water repellency increases, and contact angle approaches 90°, the meniscus curvature decreases to a minimum. Meniscus curvature reduction has been demonstrated to reduce drying rate in capillary channels similar to those used in microfluidics [*Keita et al.*, 2016]. This behavior was observed in both the HWR micromodels and simulations.

While the model was calibrated to the micromodel static contact angle, both model and experimental water films exhibited contact angle hysteresis during drying front advancement. That is, the contact angle at the invading vapor-phase front varied from the static value as the front moved through each new pore in the simulated soil geometry. LBM has been shown to replicate realistic contact angle dynamics [*Chau and Or*, 2006; *Liu et al.*, 2015].

Drying rate varied as a function of saturation within aggregated and nonaggregated micromodels. Pores within nonaggregated micromodels were randomly distributed throughout the microstructured region; in contrast, the aggregated micromodels exhibited a bimodal pore size distribution, with the largest pores interconnected and the smallest pores within particle aggregates. The largest and smallest pores within low water repellency (LWR) aggregated micromodels dried at saturation values higher than 0.5 and lower than 0.25, respectively. At saturation values higher than 0.5, LWR aggregated micromodels dried significantly faster versus LWR nonaggregated micromodels. The opposite was true at saturation values lower than 0.25; LWR aggregated micromodels dried significantly slower versus LWR nonaggregated micromodels.

Differences in capillary forces between large and small pores likely contributed to the increased drying rate at high saturation and decreased drying in low saturation within LWR aggregated micromodels. The larger pores have lower capillary forces holding water and have larger surfaces areas for evaporation, resulting in faster drying. Emulated soil particle aggregates within aggregated micromodels were positioned so that when the largest pores dried, their interaggregate micropores remained saturated but disconnected from the pores of other aggregates. This discontinuity of pores may have reduced the contribution of film flow in evaporation and evaporation became diffusion controlled at low saturation. The pores of nonaggregated micromodels were always connected hydraulically and there was not as stratified a distribution of large and small pores, resulting in a more consistent drying.

Drying rates between aggregated and nonaggregated micromodels varied with saturation in LWR micromodels, but drying rate was statistically indistinguishable between HWR aggregated and nonaggregated micromodels at all evaluated saturation ranges. Both HWR and LWR aggregated micromodels exhibited significantly lower drying rate at low (0.25–0) versus high (1–0.75) saturation. HWR nonaggregated micromodels also showed a significantly different drying rate at low versus high saturations; however, LWR nonaggregated micromodels did not show such a difference. The reduced drying rate at lower saturations and the statistical similarity between HWR aggregated and nonaggregated micromodels was likely a result

of the reduction/absence of water films. As drying progressed in both aggregated and nonaggregated micromodels, drying was diffusion controlled and drying rate decreased. Higher contact angle decreases capillary forces, allowing smaller pores to dry as larger pores dry. In HWR aggregated micromodels, reduced capillary forces allowed for a more uniform size distribution of evaporating pores, as opposed to only the largest pores evaporating first. Drying surface area in both HWR aggregated and HWR nonaggregated was similar, resulting in similar drying rates.

4.3. Dissimilarities Between Simulations and Experiments

An attempt was made to relate the LBM time scale (in time steps) to real-world time, by computing the Reynolds number for both the micromodel experiments and the LBM simulations. The Reynolds number is calculated as $Re = VL/v$, where V is front velocity, L is the particle size, and v is the kinematic viscosity. The micromodel experiments had Re in the range of 10^{-5} to 10^{-4}, while the LBM simulations had Re in the range of 10^{-3} to 10^{-2}. These values indicate that both the experiments and simulations are dominated by viscous forces rather than inertial forces, which is characteristic of most soil flow systems (except for limited cases such as preferential flow through macropores). However, the difference produces an unreasonable relationship between the experimental and simulated time scales (60,000 time steps/s). Despite this mismatch, the model faithfully recreated both the qualitative (Figure 4) and quantitative (Figure 3) behavior of the micromodels. Therefore, experimental and model results were compared on a relative time scale rather than using the Re-based scaling as is typically done [*Latt*, 2008].

LBM simulations overpredicted the effect of soil structure on drying time. Nonaggregated simulations took more than 3 times longer to dry than aggregated ones (Figure 2), depending on the relative humidity condition. In contrast, nonaggregated and aggregated soil micromodels took approximately the same amount of time to dry for the same water repellency condition (Table 1). The extended drying time for the nonaggregated simulations may be due to the increased number of pore throats through which the drying front was required to move. In the aggregated case, the invading air front moved quickly through the larger pore spaces, allowing evaporation from the intraaggregate pore space in a spatially distributed fashion. In contrast, the advancement of the front in the nonaggregated case was pinned by each subsequent pore throat, forcing evaporation to occur through a much smaller interface. Any small deviation of the LBM model from the actual evaporation kinetics of the micromodel experiments would be magnified in the nonaggregated case, resulting in much longer drying times.

4.4. Limitations of Experiments and LBM Model

Micromodels used in our experiments contained well-defined and reproducible microstructures and contact angles; however, they do not capture fully the complexity of soil. Contact angle in soil can be a dynamic property controlled by the presence of organic matter and the soil moisture regime; however, its dynamic behavior has proven difficult to replicate experimentally. Our study limited its focus to two contact angles representative of those found in the rhizosphere (higher organic matter) and bulk soil (lower organic matter). Particle sizes in soil can reach the submicron scale; fabrication of our devices can only reach a resolution of 5 μm and therefore cannot replicate the small size distribution of fine particles in soil. The spatial resolution also limits the pore sizes and porosity we can achieve within our micromodels. Micromodel resolution can be enhanced by use of advanced lithographic methods; however, the increase in resolution may be offset by cost, time, and materials. The surface treatment of PDMS by plasma to alter contact angle may introduce heterogeneities in PDMS wettability [*Karadimitriou et al.*, 2013]; functionalizing PDMS surfaces with carboxylated or aminated moieties could provide a more consistent and uniform wettability.

Our current lattice Boltzmann model estimates drying in a 2-D system, and although micromodels offer a physical pseudo-2-D environment, a three-dimensional rendering using a lattice Boltzmann code would more accurately reflect micromodel geometries. Simulations using a range of vapor-phase density boundary conditions (DBCs) have been run but have not been fully calibrated to multiple RH values. Only a single vapor-phase density was matched to our experimental RH based on validation of experimental drying kinetics. Future work could repeat drying experiments at higher RH and match LBM simulations to the observed drying kinetics to match calibrate the model for simulations of scenarios of increasing complexity.

RH variability in micromodel drying experiments may have been the result of excess water left in micromodel wells. A defined volume of water was easily added to low water repellency micromodels; however, high

water repellency micromodels required perfusion to fill with water. Although excess water was removed from micromodel wells using a pipette, excess water left in wells may have contributed to variability in relative humidity (RH). In our drying experiments, the permeability of PDMS to vapor diffusion and its ability to absorb and release moisture may have also added to RH variability. RH variability could be further controlled by attaching an in-line fan which could recirculate humidified air between the large humidity chamber and the experiment control chamber. Image resolution from our microscope camera may have also limited our capacity to measure residual saturation within dry micromodels.

5. Conclusion

Moisture retention and distribution within the rhizosphere is governed by complex and dynamic processes. Soil pore geometries are complex and difficult to consistently reproduce, while soil hydrophobicity varies spatially, temporally, and with moisture content. Our study has demonstrated that soil water repellency can exert more control over evaporative drying than soil microstructure and pore size distribution. The micromodels which were used in this study were designed based on real soil structure rather than a simplified network of pores and channels, which provided us with a more realistic view into evaporative drying patterns in soil. A LBM model was developed and validated for moisture distribution predictions in our micromodels and drying of low and high water repellency (aggregated and nonaggregated) devices at low humidity. Our soil emulating micromodel experiments have implications for understanding soil moisture and nutrient distribution in the upper portions of soil during drought, and our LBM model has potential for predicting moisture distribution and drying in the rhizosphere.

Micromodel experiments were conducted under very dry conditions, which resulted in no residual saturation at the end of each experiment. Highly water repellent (HWR) micromodels took 4 times longer versus low water repellency (LWR) micromodels to completely dry. Drying rate varied with saturation between LWR aggregated and LWR nonaggregated micromodels; however, this variation was not observed between HWR aggregated and HWR nonaggregated micromodels. Our results correspond with previous studies which indicated mixed wettability [*Bachmann et al.*, 2001; *Shahidzadeh-Bonn et al.*, 2007] and hydrophobic layers [*Shokri et al.*, 2008] in soil suppress evaporation, and contact angle can affect both drying time and kinetics [*Chapuis and Prat*, 2007; *Prat*, 2007]. Our study builds on previous studies which demonstrated evaporation from porous media can be influenced by minute differences in pore shape, contact angle, the shape of the meniscus, and the presence of film flow and capillary rings [*Keita et al.*, 2016; *Prat*, 2007; *Vorhauer et al.*, 2015].

LBM simulations predicted pore-scale moisture distribution within our complex microstructured environment under different wettability conditions. Through modification of $G_{adsorption}$ and the density boundary condition (DBC), the LBM model was able to replicate moisture distribution and drying rate as a function of saturation within HWR and LWR micromodels during drying. Moisture distribution results were compared with experimental results using a normalized characteristic length, and matched the data well. LBM simulations were conducted for DBC values ranging from 50 to 78 mu/lu². Higher humidity simulations indicated increased drying times regardless of structure. Low water repellency micromodels displayed increased residual saturation at equilibrium as LBM DBC increased. Simulation results are useful in understanding the spatial and temporal distribution of moisture within soil micromodels under complex conditions which would otherwise be difficult to test in a controlled experiment.

Increasing levels of complexity can be incorporated and controlled within soil micromodels and LBM simulations to move towards measuring and predicting moisture dynamics of the rhizosphere. Our system allows independent control of physical, chemical, and biological factors which are essential to understanding hydraulic and biophysical processes in soil. Previously we have varied solution chemistry by adding solutions of mucoid bacteria [*Deng et al.*, 2015], and used microfluidics to examine responses of bacterial biofilms to chemical gradients [*Deng et al.*, 2013]. Further studies could incorporate microscale gradients of plant exudates or localized production of mucilage, by plant roots or rhizobacteria, within micropores to study pore-scale retention of moisture near plant roots. LBM simulations can be modified to include multiple components (i.e., mucilage and exudates) to predict pore-scale moisture distribution and drying in addition to surveying a wide range of relative humidity conditions and spatially distributed water repellencies. Micromodel experiments incorporating root and microbial mucilage within different structural and wettability environments combined with LBM simulations can offer new insights into the effects of moisture dynamics on overall system function.

Macro-scale behaviors in soil are fundamentally reliant on microscale phenomena. Understanding the effects of soil microstructure and wettability on moisture distribution is important to understanding how minute differences affect the transition from stage 1 (capillary flow dominated) to stage 2 (diffusion dominated) evaporation in soil and porous media; increasing soil wettability decreases capillary forces which drastically reduces stage 1 evaporative drying, resulting in reduced macro-scale drying rates from soil. Wettability differences between adjoining soil can drastically alter the macrodistribution of moisture in soil [*Shokri and Or*, 2013]. The development of our LBM model is a step towards modeling complex moisture dynamics within soil and the rhizosphere and has implications for understanding the influence of drought on soil moisture. The distribution of soil moisture also corresponds to the distribution of nutrients and microbial hot spots in soil and is essential for understanding the function of soil in nutrient cycling.

References

Ahmed, M. A., E. Kroener, P. Benard, M. Zarebanadkouki, A. Kaestner, and A. Carminati (2016), Drying of mucilage causes water repellency in the rhizosphere of maize: Measurements and modelling, *Plant Soil*, *407*, 161–171.

Ahrenholz, B., J. Tölke, P. Lehmann, A. Peters, A. Kaestner, M. Krafczyk, and W. Durner (2008), Prediction of capillary hysteresis in a porous material using lattice-Boltzmann methods and comparison to experimental data and a morphological pore network model, *Adv. Water Resour.*, *31*(9), 1151–1173.

Aidun, C. K., and J. R. Clausen (2010), Lattice-Boltzmann method for complex flows, *Annu. Rev. Fluid Mech.*, *42*, 439–472.

Armstrong, R. T., N. Evseev, D. Koroteev, and S. Berg (2015), Modeling the velocity field during Haines jumps in porous media, *Adv. Water Resour.*, *77*, 57–68.

Bachmann, J., R. Horton, and R. Van der Ploeg (2001), Isothermal and nonisothermal evaporation from four sandy soils of different water repellency, *Soil Sci. Soc. Am. J.*, *65*(6), 1599–1607.

Bachmann, J., M.-O. Goebel, and S. K. Woche (2013), Small-scale contact angle mapping on undisturbed soil surfaces, *J. Hydrol. Hydromech.*, *61*(1), 3–8.

Bao, J., and L. Schaefer (2013), Lattice Boltzmann equation model for multi-component multi-phase flow with high density ratios, *Appl. Math. Modell.*, *37*(4), 1860–1871.

Benard, P., E. Kroener, P. Vontobel, A. Kaestner, and A. Carminati (2016), Water percolation through the root-soil interface, *Adv. Water Resour.*, *95*, 190–198.

Carminati, A. (2013), Rhizosphere wettability decreases with root age: A problem or a strategy to increase water uptake of young roots?, *Frontiers Plant Sci.*, *4*, 298.

Carminati, A., E. Kroener, M. A. Ahmed, M. Zarebanadkouki, M. Holz, and T. Ghezzehei (2016), Water for carbon, carbon for water, *Vadose Zone J.*, *15*(2).

Carminati, A., A. B. Moradi, D. Vetterlein, P. Vontobel, E. Lehmann, U. Weller, H.-J. Vogel, and S. E. Oswald (2010), Dynamics of soil water content in the rhizosphere, *Plant Soil*, *332*(1–2), 163–176.

Chapuis, O., and M. Prat (2007), Influence of wettability conditions on slow evaporation in two-dimensional porous media, *Phys. Rev. E*, *75*(4), 046311.

Chau, J. F., and D. Or (2006), Linking drainage front morphology with gaseous diffusion in unsaturated porous media: A lattice Boltzmann study, *Phys. Rev. E*, *74*(5), 056304.

Chau, J. F., D. Or, and M. C. Sukop (2005), Simulation of gaseous diffusion in partially saturated porous media under variable gravity with lattice Boltzmann methods, *Water Resour. Res.*, *41*, W08410, doi:10.1029/2004WR003821.

Czarnes, S., P. Hallett, A. Bengough, and I. Young (2000), Root-and microbial-derived mucilages affect soil structure and water transport, *Eur. J. Soil Sci.*, *51*(3), 435–443.

Deng, J., A. Dhummakupt, P. C. Samson, J. P. Wikswo, and L. M. Shor (2013), Dynamic dosing assay relating real-time respiration responses of *Staphylococcus aureus* biofilms to changing microchemical conditions, *Anal. Chem.*, *85*, 5411–5419.

Deng, J., E. P. Orner, J. F. Chau, E. M. Anderson, A. L. Kadilak, R. L. Rubinstein, G. M. Bouchillon, R. A. Goodwin, D. J. Gage, and L. M. Shor (2015), Synergistic effects of soil microstructure and bacterial EPS on drying rate in emulated soil micromodels, *Soil Biol. Biochem.*, *83*, 116–124.

Dye, A. L., J. E. McClure, D. Adalsteinsson, and C. T. Miller (2016), An adaptive lattice Boltzmann scheme for modeling two-fluid-phase flow in porous medium systems, *Water Resour. Res.*, *52*, 2601–2617, doi:10.1002/2015WR018279.

Furrer, J. M., and A. C. Bagtzoglou (2017), Pore-scale modeling of water-phase fragmentation in simulated soils with realistic pore geometry, *Granular Matter*, *19*(2), 19.

Gray, W. G., A. Dye, J. McClure, L. Pyrak-Nolte, and C. T. Miller (2015), On the dynamics and kinematics of two-fluid-phase flow in porous media, *Water Resour. Res.*, *51*, 5365–5381, doi:10.1002/2015WR016921.

Haussels, R., T. Klenke, J. Kropp, and W. Ebenhöh (2001), Investigations on the influence of pore-space geometry on concentration patterns and transportation properties of dissolved oxygen in a bioactive sandy sediment by a lattice Boltzmann automaton model, *Hydrol. Processes*, *15*(1), 81–96.

Karadimitriou, N., M. Musterd, P. Kleingeld, M. Kreutzer, S. Hassanizadeh, and V. Joekar-Niasar (2013), On the fabrication of PDMS micromodels by rapid prototyping, and their use in two-phase flow studies, *Water Resour. Res.*, *49*, 2056–2067, doi:10.1002/wrcr.20196.

Karadimitriou, N., S. Hassanizadeh, V. Joekar-Niasar, and P. Kleingeld (2014), Micromodel study of two-phase flow under transient conditions: Quantifying effects of specific interfacial area, *Water Resour. Res.*, *50*, 8125–8140, doi:10.1002/2014WR015388.

Keita, E., S. A. Koehler, P. Faure, D. A. Weitz, and P. Coussot (2016), Drying kinetics driven by the shape of the air/water interface in a capillary channel, *Eur. Phys. J. E*, *39*(2), 1–10.

Landry, C., Z. Karpyn, and O. Ayala (2014), Relative permeability of homogenous-wet and mixed-wet porous media as determined by pore-scale lattice Boltzmann modeling, *Water Resour. Res.*, *50*, 3672–3689, doi:10.1002/2013WR015148.

Latt, J. (2008), *Choice of Units in Lattice Boltzmann Simulations*, Palabos LBM Wiki. [Available at http://lbmethod.org/_media/howtos:lbunits.pdf.]

Li, Y., E. J. LeBoeuf, P. K. Basu, and S. Mahadevan (2005), Stochastic modeling of the permeability of randomly generated porous media, *Adv. Water Resour.*, *28*(8), 835–844.

Liu, H., Y. Ju, N. Wang, G. Xi, and Y. Zhang (2015), Lattice Boltzmann modeling of contact angle and its hysteresis in two-phase flow with large viscosity difference, *Phys. Rev. E*, *92*(3), 033306.

Liu, Y., D. Nolte, and L. Pyrak-Nolte (2011), Hysteresis and interfacial energies in smooth-walled microfluidic channels, *Water Resour. Res.*, *47*, W01504, doi:10.1029/2010WR009541.

Luo, L.-S. (2000), Theory of the lattice Boltzmann method: Lattice Boltzmann models for nonideal gases, *Phys. Rev. E*, *62*(4), 4982.

Markov, D. A., P. C. Samson, D. K. Schaffer, A. Dhummakupt, J. P. Wikswo, and L. M. Shor (2010a), Window on a microworld: Simple micro-fluidic systems for studying microbial transport in porous media, *J. Visualized Exp.*, *39*, doi:10.3791/1741.

Markov, D. A., S. Manuel, L. M. Shor, S. R. Opalenik, J. P. Wikswo, and P. C. Samson (2010b), Tape-underlayment, rotary-node (TURN) valves for simple on-chip microfluidic flow control, *Biomed. Microdev.*, *12*(1), 135–144.

Martys, N. S., and H. Chen (1996), Simulation of multicomponent fluids in complex three-dimensional geometries by the lattice Boltzmann method, *Phys. Rev. E*, *53*(1), 743.

Moebius, F., and D. Or (2012), Interfacial jumps and pressure bursts during fluid displacement in interacting irregular capillaries, *J. Colloid Interface Sci.*, *377*(1), 406–415.

Moradi, A. B., A. Carminati, A. Lamparter, S. K. Woche, J. Bachmann, D. Vetterlein, H.-J. Vogel, and S. E. Oswald (2012), Is the rhizosphere temporarily water repellent?, *Vadose Zone J.*, *11*(3).

Münster, S. and B. Fabry (2013), A simplified implementation of the bubble analysis of biopolymer network pores, *Biophys J.*, *104*(12), 2774–2775.

Olson, M. S., R. M. Ford, J. A. Smith, and E. J. Fernandez (2004), Quantification of bacterial chemotaxis in porous media using magnetic reso-nance imaging, *Environ. Sci. Technol.*, *38*(14), 3864–3870.

Or, D., B. F. Smets, J. Wraith, A. Dechesne, and S. Friedman (2007), Physical constraints affecting bacterial habitats and activity in unsatu-rated porous media—A review, *Adv. Water Resour.*, *30*(6), 1505–1527.

Or, D., P. Lehmann, E. Shahraeeni, and N. Shokri (2013), Advances in soil evaporation physics—A review, *Vadose Zone J.*, *12*(4).

Prat, M. (2007), On the influence of pore shape, contact angle and film flows on drying of capillary porous media, *Int. J. Heat Mass Transfer*, *50*(7), 1455–1468.

Pyrak-Nolte, L. J., D. D. Nolte, D. Chen, and N. J. Giordano (2008), Relating capillary pressure to interfacial areas, *Water Resour. Res.*, *44*, W06408, doi:10.1029/2007WR006434.

Qian, Y., D. d'Humières, and P. Lallemand (1992), Lattice BGK models for Navier-Stokes equation, *Europhys. Lett.*, *17*(6), 479.

Roman, G. T., and C. T. Culbertson (2006), Surface engineering of poly (dimethylsiloxane) microfluidic devices using transition metal sol-gel chemistry, *Langmuir*, *22*(9), 4445–4451.

Rubinstein, R. L., A. L. Kadilak, V. C. Cousens, D. J. Gage, and L. M. Shor (2015), Protist-facilitated particle transport using emulated soil micromodels, *Environ. Sci. Technol.*, *49*(3), 1384–1391.

Schindelin, J., I. Arganda-Carreras, E. Frise, V. Kaynig, M. Longair, T. Pietzsch, S. Preibisch, C. Rueden, S. Saalfeld, and B. Schmid (2012), Fiji: An open-source platform for biological-image analysis, *Nat. Methods*, *9*(7), 676–682.

Schwartz, N., A. Carminati, and M. Javaux (2016), The impact of mucilage on root water uptake—A numerical study, *Water Resour. Res.*, *52*, 264–277, doi:10.1002/2015WR018150.

Shahidzadeh-Bonn, N., A. Azouni, and P. Coussot (2007), Effect of wetting properties on the kinetics of drying of porous media, *J. Phys. Con-dens. Matter*, *19*(11), 112101.

Shan, X., and H. Chen (1994), Simulation of nonideal gases and liquid-gas phase transitions by the lattice Boltzmann equation, *Phys. Rev. E*, *49*(4), 2941.

Shokri, N., and D. Or (2011), What determines drying rates at the onset of diffusion controlled stage-2 evaporation from porous media?, *Water Resour. Res.*, *47*, W09513, doi:10.1029/2010WR010284.

Shokri, N., and D. Or (2013), Drying patterns of porous media containing wettability contrasts, *J. Colloid Interface Sci.*, *391*, 135–141.

Shokri, N., P. Lehmann, and D. Or (2008), Effects of hydrophobic layers on evaporation from porous media, *Geophys. Res. Lett.*, *35*, L19407, doi:10.1029/2008GL035230.

Shokri, N., P. Lehmann, and D. Or (2009a), Characteristics of evaporation from partially wettable porous media, *Water Resour. Res.*, *45*, W02415, doi:10.1029/2008WR007185.

Shokri, N., P. Lehmann, and D. Or (2009b), Critical evaluation of enhancement factors for vapor transport through unsaturated porous media, *Water Resour. Res.*, *45*, W10433, doi:10.1029/2009WR007769.

Singh, R., and M. S. Olson (2011), Transverse mixing enhancement due to bacterial random motility in porous microfluidic devices, *Environ. Sci. Technol.*, *45*(20), 8780–8787.

Stalder A. F., G. Kulik, D. Sage, L. Barbieri, P. Hoffmann (2006), A snake-based approach to accurate determination of both contact points and contact angles, *Colloid. Surfaces A.*, *286*(1-3), 92–103.

Stanley, C. E., G. Grossmann, and X. C. i Solvas (2016), Soil-on-a-Chip: Microfluidic platforms for environmental organismal studies, *Lab Chip*, *16*(2), 228–241.

Sukop, M. C., and D. Or (2003), Invasion percolation of single component, multiphase fluids with lattice Boltzmann models, *Phys. B: Condens Matter*, *338*(1), 298–303.

Sukop, M. C., and D. Or (2004), Lattice Boltzmann method for modeling liquid-vapor interface configurations in porous media, *Water Resour. Res.*, *40*, W01509, doi:10.1029/2003WR002333.

Sukop, M. C., H. Huang, C. L. Lin, M. D. Deo, K. Oh, and J. D. Miller (2008), Distribution of multiphase fluids in porous media: Comparison between lattice Boltzmann modeling and micro-x-ray tomography, *Phys. Rev. E*, *77*(2), 026710.

Tang, Y., A. J. Valocchi, C. J. Werth, and H. Liu (2013), An improved pore-scale biofilm model and comparison with a microfluidic flow cell experiment, *Water Resour. Res.*, *49*, 8370–8382, doi:10.1002/2013WR013843.

Tracy, S. R., K. R. Daly, C. J. Sturrock, N. M. Crout, S. J. Mooney, and T. Roose (2015), Three-dimensional quantification of soil hydraulic prop-erties using X-ray Computed Tomography and image-based modeling, *Water Resour. Res.*, *51*, 1006–1022, doi:10.1002/2014WR016020.

Traoré, O., V. Groleau-Renaud, S. Plantureux, A. Tubeileh, and V. Boeuf-Tremblay (2000), Effect of root mucilage and modelled root exu-dates on soil structure, *Eur. J. Soil Sci.*, *51*(4), 575–581.

Vorhauer, N., Y. Wang, A. Kharaghani, E. Tsotsas, and M. Prat (2015), Drying with formation of capillary rings in a model porous medium, *Transp. Porous Media*, *110*(2), 197–223.

Yoon, H., A. J. Valocchi, C. J. Werth, and T. Dewers (2012), Pore-scale simulation of mixing-induced calcium carbonate precipitation and dis-solution in a microfluidic pore network, *Water Resour. Res.*, *48*, W02524, doi:10.1029/2011WR011192.

Zarebanadkouki, M., M. A. Ahmed, and A. Carminati (2015), Hydraulic conductivity of the root-soil interface of lupin in sandy soil after dry-ing and rewetting, *Plant Soil*, *398*(1), 267–280.

Zou, Q., and X. He (1997), On pressure and velocity boundary conditions for the lattice Boltzmann BGK model, *Phys. Fluids*, *9*(6), 1591–1598.